Co-evolution of spheroid fluidization and mechanical fracture in a morphogenic cascade

Selwin K. Wu[1,2], Celestine Z. Ho[1,8], Fuqiang Sun[3,8], Yuting Lou[1,8], Christina Bao-Xian Huang[1], Jingwei Xiao[1], Murat Shagirov[1], Ivan Yow[1], Jasmine Fei Li Chin[1], Suzie Verma[4], Alpha S. Yap[4], Yuan Lin[3,5], Tetsuya Hiraiwa[1,6], Boon Chuan Low[1,2,7]

[1]Mechanobiology Institute, National University of Singapore, Singapore
[2]Department of Biological Sciences, National University of Singapore, Singapore
[3]Department of Mechanical Engineering, University of Hong Kong, Hong Kong, China
[4]Institute for Molecular Bioscience, University of Queensland, Brisbane, Australia
[5]Advanced Biomedical Instrumentation Centre, Hong Kong Science Park, Shatin, New Territories, Hong Kong, China
[6]Present address: Institute of Physics, Academia Sinica, Taipei, Taiwan
[7]NUS College, National University of Singapore, Singapore

[8]Contributed Equally
*Correspondence: dbslowbc@nus.edu.sg & ylin@hku.hk (fracture analysis) & selwinwu@nus.edu.sg

Abstract

Cell collectives can undergo solid to fluid states transition and break apart during development and disease. How these processes coordinate collective cell invasion of a tissue barrier, as well as the underlying biological and physical principles, remains unclear. Using a three-dimensional model system of cancer spheroids invading the mesothelium, we find that the mesothelial cell-cell contacts undergo tensile fracturing as the spheroid invades. This tensile fracture is triggered by mesothelial cell apical constriction, a consequence of intercellular integrin complex engagement between the spheroid leader cell and the mesothelial cell. Concurrently, persistent directed migration of spheroid cells propagate the mesothelial fracture. In response, the deformed mesothelium exerts resisting forces on the fluidizing spheroid, leading to a crowding effect and contact inhibition of the fluidizing spheroid. We have uncovered a morphogenic cascade, revealing that the invasion of cells into adjacent cellular and extracellular matrix-rich microenvironment emerges from the co-evolution of spheroid fluidization and mesothelium fracture triggered by intercellular integrin complex engagement.

Introduction

Collective migration and heterotypic interactions between multicellular assemblies drive morphogenic transformation in both tissue development and cancer progression [1-3]. For example, a critical step for Drosophila oogenesis entails border cell clusters interacting with their surrounding nurse cells, which promotes the migration of the border cell clusters towards the oocyte[4, 5]. In cancer, tumour spheroids penetrate tissues through tight interstitial spaces, ultimately colonizing distal peritoneal organs[5, 6]. Here, we study the 3D heterotypic culture model that mimics ovarian tumour invasion of the mesothelium during peritoneal metastatic implantation[7-10]. Notably, the spreading of cancer spheroid has also been used to study the wetting process[11-13]. The mesothelium is a monolayer of simple squamous epithelium that lines the body's internal organs and serous cavities, such as the lungs and omentum[14]. As such, organs within the peritoneal cavity are covered with mesothelium[15-17]. Previous electron micrograph studies of patients' ovarian tumours attached to the peritoneum revealed that mesothelial cells were absent beneath the invading tumor[6, 16-18], implying that clearing of mesothelium by cancer spheroids is an early step of ovarian metastatic colonization. In 3D cultures, it was suggested that α5 integrin and Talin-dependent activation of non-muscle myosin-II was required for the spheroid to displace the mesothelial cells apart during invasion[7, 8]. However, the underlying biophysical principles and cellular mechanisms remains unclear. Here, we present a new collective invasion model that emerges from the co-evolution of spheroid fluidization and mesothelium fracture.

Fracture initiation of the mesothelium is akin to crazing during spheroid invasion

The human ovarian adenocarcinoma OVCA433 epithelial cells were cultured to form spheroids in suspension, bearing a grape cluster-like morphology (Fig. 1a)[19]. The wild-type OVCA433 cells exhibited a epithelia morphology when grown as a monolayer. The OVCA433 spheroids were introduced onto the ZT mesothelia[9] which express E-cadherin tdTomato (Fig. 1a).

As spheroids invaded the mesothelium, a phenomenon akin to thermoplastic polymer crazing was observed at the mesothelial cadherin junctions (Fig. 1a' and Video 1). Crazing is a unique feature when thermoplastic polymer materials fracture[20], characterized by a network of fine cracks within the material. It occurs when excessive tensile stress or "stretching" is applied to a polymer, producing gaps termed as fibrillar bridges, which are thought to help sustain some of the stress. (Fig. 1a'' and Video 1).

At the mesothelium, we observed the fibrillar bridges of intercellular adhesion molecule, E-cadherin, and formation of microvoids similar to crazing, prior to the complete mesothelial fracturing from cadherin bridges rupturing (Fig 1a'' and Video 1). Mesothelial fracture initiation was also characterized by the elongation of E-cadherin puncta and we did not observe any dramatic reduction of E-cadherin at the intact areas of the mesothelium during crazing (Fig. 1a''', Video 1). These craze-like features are not specific to mesothelium cultured on glass, as we observe fibrillar bridges at sites of spheroid invasion when mesothelium is grown on matrigel (Video 2).

Analogous to crazing in thermoplastics, the fibrillar bridges that formed during mesothelium fracture initiation might have resisted fracture propagation (Figure 1a, Video 1 & 2). Thus, we investigated this possibility by specifically weakening cell-cell contacts. RhoA-Myosin-II mediated contractility supports E-cadherin cell-cell adhesion strength[21-24]. Hence, we reduced E-cadherin adhesiveness of the mesothelium by expressing a dominant negative RhoA mutant T19N fused to E-cadherin(Figure 1b and Supplementary Figure 1a). Strikingly, the craze-like structures that formed during spheroid invasion were reduced in the mesothelium expressing E-cad-RhoA-T19N mutant (Fig. 1c,d). Although the rate of spheroid-induced mesothelial fracture remains unchanged in mesothelium expressing the E-cad-RhoA-T19N mutant (Supplementary Fig. 1b), more extensive mesothelial clearance by spheroid invasion were observed in these cells (Fig. 1e). Thus, these E-cadherin linked fibrillar bridges may resist mesothelium clearance by the invading spheroid.

Tensile fracture of the mesothelium by spheroid engagement

To directly analyse the fracturing process in the mesothelium, we tagged its apical surface with fluorescent microbeads[25] and imaged it undergoing spheroid invasion. 500nm beads were coated with WGA for binding to the cell surface[25].

A material's fracture response can be classified as brittle or more ductile in nature according to the extent of its deformation during fracture. A ductile fracture is seen in readily deformable materials and characterized by extensive plastic deformation that occurs before the material finally breaks apart[26]. By contrast, a brittle fracture exhibits little or no plastic deformation before its fracture[26]. Velocity magnitude quantification from particle image velocimetry (PIV)

of the WGA-coated beads on the mesothelium apical surface revealed significant deformation of the mesothelium (Fig. 1f). This suggest that the tearing of the mesothelium is akin to ductile fracture. Additionally, we did not detect any behaviour that reflects ductile to brittle transition as the sizes of deformation zones associated with fracture initiation and propagation are similar (Fig. 1g,h,i). This suggested that significant energy was absorbed by the deformed mesothelium throughout spheroid invasion and spreading.

Furthermore, there are three principal modes by which fracture occurs, namely tensile fracture (mode I), shear fracture (mode II) and out-of-plane tearing (mode III). Since crazes typically form at the plane normal to tensile stress[27], spheroid invasion should most likely induce mesothelial tensile fracture.

Indeed, PIV of the beads on the mesothelium apical surface after spheroid invasion revealed that there was a constriction zone right next to the region where crack was initiated (Fig. 1f). The small crack opens up a hole in the middle of the mesothelium after being pulled from both sides, an indication of a tensile fracture. A larger displacement of the beads at one side of the tensile fracture reveals anisotropy in the tensile fracture.

Given that cells did not evidently slide past each other upon crazing, it is unlikely that in-plane shear is an important driver of fracture initiation (Fig. 1a). To quantify the deformation nature of the mesothelium, we examined both the normal strain rate and shear strain rate of the mesothelium undergoing fracture (Fig. 1f). Here the normal strain rate represents the strength of velocity gradient in the direction of the local velocity and the shear strain rate represents the strength of velocity gradient perpendicular to the local velocity[28]. Physically, a high shear rate near the fracturing site means the fracture is largely dominated by in-plane shear. On the other hand, a vanishing/small shear rate with high expansion velocity corresponds to tensile fracture (Methods).

Despite the higher flowing velocity of cells near the fracture compared to other areas away from the site of fracture, such difference was not observed in the shear rate distribution (Fig. 1f). Thus, fracture initiation and propagation in mesothelium are tensile-mode dominated. Later, strong heterogeneity in the distribution of shear rate was found near the fracture in the later stage of fracture propagation (Fig. 1f, 1k, Video 3), indicating the portion of in-plane shearing has increased during the propagation of mesothelial fracture.

Finally, using lattice light sheet microscopy to achieve a clear cross section view, we did not observe any out-of-plane tearing (mode III) of the mesothelium caused by the spheroid (Fig. 1l). Additionally, protrusions were mostly observed after mesothelial fracture. Protrusions penetrating the mesothelium E-cadherin junctions preceding mesothelial fracture were only observed in ~6% of the invading spheroids (Supplementary Fig. 1c). While in majority of the spheroids, their protrusions were formed after mesothelial fracture. Indeed, lattice light sheet imaging revealed that mesothelial cells were forced apart from the apical side first and such separation then propagated to the basal side leading to complete fracture of the mesothelium. Thus, tensile fracture is the principal mode initiating spheroid-induced mesothelial fracture.

Spheroid-induced mesothelial cell apical constriction initiates tensile fracture of the mesothelium

We then investigated the cellular mechanism underlying tension-induced mesothelial fracture by spheroids. We observed apical constriction of a mesothelial cell beneath the spheroid as the mesothelium begins to fracture (Fig. 2a). By contrast, such aggressive apical constriction is not detected in the other areas of the intact mesothelium away from any fracture sites as shown by a more constant cell apical area (Fig. 2b). It is conceivable that apical constriction of a cell could stretch its junctions with neighbouring cells and eventually result in the aforementioned tensile fracture (Fig. 1f). Apical constriction is a cell shape deformation mechanism promoting tissue remodelling during development[29-32] that is triggered by increased activation of myosin-II at the apical cortex[23, 31, 33, 34]. Structured illumination super-resolution imaging of myosin-regulatory-light-chain (MRLC)[35] revealed a myosin-II network extending across the apical region of the mesothelial cells (Fig. 2c, c'). In quantitative live-imaging, MRLC intensifies at the junctional and apical cortex region of a mesothelial cell beneath the interacting spheroid (Fig. 2a,d and Video 4) such that intensification of MRLC precedes junction constriction and fracture (Fig. 2d). Thus, supporting the notion that constriction of apical mesothelial myosin-II cortex exerts an anisotropic pull on E-cadherin junctions, causing mesothelial fracture initiation.

Besides the apical constriction mechanism, we use traction force microscopy (TFM) to analyse the contribution of in-plane traction-mediated migration of mesothelial cells during fracture[25, 36]. First, we find that the spheroid's leader cell tends to contract the PDMS substrate in the absence of mesothelium (Fig. 2e,f). Next, we introduced a spheroid on the mesothelium grown

on PDMS but failed to detect an enhancement in the mesothelial cell traction force on the PDMS substrate (Fig. 2g,h) or any change in radial traction stress of mesothelial cells upon fracture initiation (Fig. 2g,i). Thus, it is unlikely that the traction-mediated lateral migration of mesothelial cells away from the invading spheroid initiated fracture[7].

Intercellular and apical integrins trigger mesothelial fracture and collective cell invasion

We hypothesize that heterotypic interactions trigger mesothelial apical constriction. It was shown that mesothelial clearance is initiated by ovarian tumour attachment to the mesothelium via integrin alpha-5[7, 8], but the organization of intercellular integrin-matrix complexes in a 3D microenvironment remains unclear. To visualize the intercellular integrin-matrix complexes, we imaged Paxillin - a key component of the integrin matrix adhesion at the spheroid-mesothelium contact region. Strikingly, when they attached to the mesothelium, spheroids expressing paxillin-GFP exhibited strands of paxillin-GFP at the spheroid-mesothelium interface (Fig. 3a, Supplementary Fig. 3a), which grew from smaller, initial spots (Fig. 3b). The mesothelium tends to fracture before a spheroid's leader cell fully spread on a mesothelial cell (Supplementary Fig. 3b). These strands of paxillin morphologically resemble the integrin adhesion complexes seen when cells spread on artificial substrates[37]. We observed that mesothelial fracture occurred after partial spreading of a spheroid's leader cell on the mesothelium in ~70% of invasion cases (Supplementary Fig. 3b).

As E-cadherin interactions between the heterotypic epithelial assemblies[3, 4, 33, 38, 39] was undetected with colocalization analysis between E-cad GFP spheroid and Ecad tdT mesothelium (Fig 3c,d) , we continued to analyse the functional importance of integrin instead. Knocking down α5β1 integrin and using a thrombospondin-1 (TSP-1) peptide[40] to specifically block fibronectin-based adhesion of cells successfully blocked mesothelial fracture by the spheroid (Fig. 3e-g, Supplementary Fig. 3c,d), validating the role of α5 integrin in the spheroid-mesothelium attachment.

It is possible that integrin adhesion receptors are present at the apical surface of mesothelial cells, mediating their attachment to the spheroid. Our speculation stemmed from spheroid invasion experiments where we introduced mesothelial cell doublets to attach onto a round fibronectin micropattern (Fig. 3h). Despite the confinement of matrix adhesive area, the mesothelial cells detached from the adhesive pattern and remained with the spheroid at the non-

adhesive region of the substrate (Fig. 3h), whereas in areas without spheroid the mesothelial cells remained attached on the adhesive round micropattern (Supplementary Fig. 3e). This observation was consistent with our TFM data, together suggesting that mesothelial cell's outward migration away from the spheroid by basal traction is dispensable for mesothelial fracture.

Apical integrin adhesion complexes have been reported for the blastoderm to attach on the vitelline envelope during insect gastrulation[41], albeit without direct visualization of these integrins. Here, strands of paxillin were localized at the apical side of mesothelial cells and exhibited colocalization with immunostained fibronectin (Fig. 3i). Even in the absence of spheroid attachment to the apical side of the mesothelium, α5 integrin and other binding partners of the integrin complex, including Paxillin, kank2, tensin1, fibronectin and vinculin, colocalized at sites of apically localized integrin-based adhesions (Fig. 3j). Both mesothelial i α5 integrin and mesothelial fibronectin knockdown respectively was sufficient to block spheroid-induced fracture (Fig. 3k & l, Supplementary Fig. 3f-i and Video 5). Of note, knockdown of α5 integrin primarily depleted apical integrins with subtle reduction of basal integrins (Supplementary Fig. 3h). Thus, the mesothelium's apical integrin adhesion complex is required for spheroid invasion.

Our evidence supports the notion that mesothelial apical constriction from intercellular integrin engagement initiates the mesothelium tensile fracture. To directly test this, we blocked spheroid-induced mesothelial apical constriction, by linking a dominant-negative RhoA mutant to α5 integrin (Fig. 3m and Supplementary Fig. 3j-l). This led to the reduction of spheroid-induced mesothelial fractures (Fig. 3n & o and Video 5). Thus, intercellular integrin engagement induces mesothelial fracture in part by apical myosin-II activation. This is surprising as major cell-cell adhesion molecules such as the cadherin family is the more well-studied direct mechanotransducer between epithelial cells instead[33].

Fluidization and directed collective motility of contact-inhibited invading spheroids

Successful spheroid invasion and spreading on the submesothelial substrate can promote spheroid survival by preventing detachment and anoikis of spheroids[42] (Fig. 4a). Since the mesothelium fracture exhibits ductile behaviours(Fig. 1f-i), the fracturing mesothelium may absorb some of the spreading force exerted by the spheroid to retard fracture propagation.

Indeed, we found that the spheroid spreading was significantly retarded when it occured along a fractured mesothelium (Fig. 4b,c, Video 6). In the absence of the mesothelium, the spheroid spreads freely (Video 7). Thus, the mesothelium retards but does not promote spreading of the spheroids. This is in agreement with our evidence that mesothelial E-cadherin fibrillar bridges contributes to spheroid spreading resistance (Fig.1e).

To assess the spheroid cell dynamics influencing mesothelial fracture propagation and their motility patterns, we quantitatively compared the cellular motility of (1) invading spheroids with (2) non-invading spheroids as a result of ITGA5 knockdown in the mesothelium and (3) spheroids spreading in the absence of the mesothelium-where we termed it as freely-spreading spheroid. We obtained tracking data of the spheroid's cell nuclei by deep-learning segmentation[43] and IMARIS tracking (Fig. 4d,e, Supplementary Fig. 4a,b). We first compare (1) invading spheroids with (2) non-invading spheroids- by knocking down ITGA5 in the mesothelium, to identify the motility patterns induced by intercellular integrin adhesion engagement. Strikingly, in XZ and RZ (radial Z) velocity maps generated from 3D cell tracking and quantitative velocity analysis, there was an overall bias in spheroid cell movement towards the mesothelium base, even before mesothelial fracture (Fig. 4f,g, Video 8). However the spheroids that did not invade due to mesothelium ITGA5 knockdown, exhibit a random cellular motion instead (Fig. 4f,g). Thus, intercellular α5 integrin engagement induces collective motility of spheroid cells towards the mesothelium prior to mesothelium fracture.

We then assessed whether directed cell migration is involved during invasion. We quantified the velocity auto-correlation of these spheroid cells after mesothelial fracture and detected a significant increase in the persistency of the velocity auto-correlations of invading spheroid cells when compared with non-invading spheroid cells (Fig. 4h). Strikingly, the velocity auto-correlation persistency in free-spreading spheroid was significantly higher than that in spheroid invasion. Thus, the invading spheroid cells exhibited persistent directed motility, which was further enhanced with the removal of the mesothelium barrier (Fig. 4h).

The transition of non-invading spheroid cells from being randomly motile to invading spheroid cells moving in a directed manner may reflect the induction of supracellular fluidization[44]. Fluidization is the transition of cell collectives from a jammed to an unjammed state, orchestrating collective migration[45, 46]. Thus, we compare the mean squared displacement (MSD) of spheroid cells, which is a critical parameter in distinguishing jammed from

unjammed states[47]. To circumvent any fluctuations introduced by spheroid drift, we quantified the pair-wise MSD of spheroids (Methods). We found that at long lag-time of fifty minutes, the pair-wise MSD slope values of the invading spheroid are ≥1 (Fig. 4j). We observed a gradient of increasing supracellular diffusive motion, from the diffusive top to its super-diffusive base (Fig. 4j). It is thought that super-diffusion or ballistic motion of cells usually corresponds to single cell migration. We find that the base of the invading spheroid was spreading as a continuous layer even when exhibiting a supracellular ballistic motion (Video 6). In contrast, when invasion was prevented by mesothelial ITGA5 KD, cells in the non-invading spheroid were found to move at a sub-diffusive rate, indicative of a jammed motion (Fig. 4j). Thus, apical mesothelium α5 integrin is required for spheroid fluidization.

During spheroid invasion of the mesothelium, cells flow like fluid at long timescales. At short timescales, cells usually remain less-motile and solid-like, with the motion of each cell constrained by cell crowding from its neighbours[48, 49]. To identify potential crowding effect on the invading spheroid, we analysed the spheroid cell motility at short timescales. Strikingly, at the short lag-time of 10 minutes, we observed a more sub-diffusive supracellular motion from the pair-wise MSD analysis in the base region of both invading and non-invading spheroids when compared to freely-spreading spheroid (Fig. 4j). This increase in sub-diffusiveness at a lag time of ten minutes might be due to confinement from the fracturing mesothelium retarding spheroid spreading. This was confirmed by quantifying the ratio of cell velocities at ~10 minutes lag-time standard deviation between XY plane over the Z plane, revealing a reduced ratio in invading spheroids when compared to the spreading spheroids (Fig. 4k). This is in agreement with our MSD slope data at short lag time, together suggesting a motion constraint at the bottom region of invading spheroids as compared to freely-spreading spheroid.

The motion constraint of invading spheroid cells at ten minutes lag time could reflect cellular crowding. Thus, we assessed crowding on the spheroid spreading within the fracturing mesothelium by k-nearest neighbours algorithm (KNN) analysis. As expected, the spheroid exhibited increasing cell density over time as it spread to propagate the mesothelial fracture (Fig. 4l). By contrast, the cellular density of a non-invading and freely-spreading spheroid remained constant (Fig. 4l). Additionally, the spheroids experiencing crowding are contact inhibited at the lower region of the spheroids, as their proliferative potential has been reduced at the spheroid base as indicated by a decrease in nuclear Ki67 (Fig. 4m, n) and lower nuclear-to-cytoplasmic ratio of Yap (Fig. 4o and Supplementary Fig. 4c).

Of note, cancer cells often enter dormancy characterised by low proliferative potential as they metastasize to a new secondary site[50]. Consistent with this idea, cancer spheroids experience crowding as they propagate the mesothelial fracture. This resulted in spheroid cells with a lower proliferative potential (Fig. 4m,n,o). Thus, it is tempting to speculate that crowding mediated contact inhibition may in some cases contribute to dormancy. Indeed, this has been assumed in previous theoretical modelling of cancer studies[51]. Cancer cell dormancy typically invokes critical clinical implications, as these cells often evade treatment and contribute to cancer relapse[50]. This is because non-dividing cancer cells tend to evade cancer therapies which mostly kill rapidly dividing cells, subsequently cancer cells that evaded treatment contribute to relapse years after treatment[50].

Overall, we conclude that spheroid invasion of the mesothelium emerges from the co-evolution of spheroid fluidization and fracture. We have presented several properties of this emergent phenomenon, this includes the intercellular adhesion strength of the mesothelium, the fracture response of the mesothelium and the directedness of the spheroid cells motility.

The mesothelium provides the opportunity for the spheroid to initiate invasion by presenting fibronectin fibrils on its apical integrin. By contrast, during mesothelial clearance the mesothelium exerts an invasion inhibitory role by resisting spheroid spreading. The mechanism for spheroid that spreads freely, termed active wetting, involves the increasing spheroid cell substrate interactions and traction forces which outcompete the E-cadherin induced intercellular stresses during spreading[11, 12]. In our experiments, the mesothelial cell neighbours might also compete with the spreading spheroid for cell-substrate interactions. Ultimately, reinforcing contact inhibition of the invading spheroid by promoting cellular crowding.

As hypothesized by D'Arcy Thompson a century ago[52], the shaping of tissues shares physical principles with the sculpting of non-living materials, where transitions between solid and fluid states mould them into functional shapes. The crosstalk between fluidization with fracture likely yield even more diverse supracellular structures, leading to varied tissue physical properties and functionalities. Here we have identified fluidization with crowding as one consequence. We propose that the co-evolution of supracellular fluidization and fracture may represent a general mechanism for collective locomotion of cells into adjacent cellular and extracellular matrix-rich microenvironment.

Figures

Figure 1. Spheroid-induced mesothelial tensile fracture.

(a) Mesothelial E-cadherin contact exhibits fracture initiation akin to "crazing" upon spheroid invasion. Representative time-lapse images of the mesothelium that is under a spheroid (colour coded in hot orange). a'-a''' with detailed views. a''' shows a cadherin fibrillar bridge being extended as crazing proceeds. Red arrows point towards a fibrillar extension and green arrows point towards a microvoid.

(b) Schematic of E-cad-GFP-RhoA-T19N fusion protein.

(c,d) Reduction of E-cad 'crazing' during mesothelial fracture when E-cad based contractility is reduced. Representative images (c) and quantification (d) of the percentage of mesothelium E-cad fibrillar bridges when either RhoA-T19N mutant is fused to E-cad or in controls.

(e) Increased in mesothelial clearance when E-cadherin adhesion is compromised. Quantitative comparison of the mesothelial clearance size when either RhoA-T19N mutant is fused to mesothelial E-cad or in controls.

(f) Tension-induced fracture. PIV analysis of fluorescent microbeads on top of the mesothelium expressing Ecad-tdTomato. The heatmaps of simple shear rate (s^{-1}) or simple strain rate (s^{-1}) or velocity(µm/s) from the PIV analysis. Right magnified view of the velocity PIV heatmap show outward vectors away from the site of fracture initiation(grey dotted circle).

(g,h) Velocity magnitude line scan of area beside fracture initiation(g) or fracture(h).

(i) Comparison of process zone size between fracture initiation and fracture. Data representative of two independent experiments.

(j) Diagram of three different modes of fracture which the mesothelium may undergo. The modes are Mode I: Opening (stress orthogonal to the local plane of the crack surface), Mode II: In-plane-shear (stress parallel to the crack surface but orthogonal to the crack front), and Mode III: Out-of-plane shear (stress parallel to the crack surface and to the crack front). The arrows indicate the direction of stress and asterisks indicate that point of crack.

(k) Tension-induced fracture is the dominant initiating mode of fracture. Comparison between the fold changes of the simple shear rate and simple strain rate with velocity magnitude analysis during fracture initiation and fracture.

(l) Mode III: Out-of-plane shear fracture is not detected when spheroid begins to invade the mesothelium. XZ views of time-lapse lattice light-sheet microscopy images of E-cad GFP spheroid invading E-cad tdT mesothelium. Grey arrows indicate the opening of mesothelial cell-cell contacts.

All data are means ± SEM from at least n=2 independent experiments, except for (d) which are from n=8 independent experiments, ns, not significant, *p < 0.05, **p < 0.01, ****p < 0:0001; analysed with unpaired t-test. Scale bars, 5μm.

Figure 2. Initiation of fracture from apical constriction of mesothelial cell.

(a,b,c,d) Apical constriction precedes fracture initiation of mesothelium. (a)Time-lapse images of spheroid (brightfield, top right) invading mesothelium expressing E-cad tdT and MRLC-GFP. Intensification of MRLC filaments is observed as apical constriction of mesothelial cell led to subsequent fracture initiation of mesothelium. (b) Variance quantification of mesothelial apical cell area beneath spheroid during fracture compared to areas not undergoing fracture. (c) Network of myosin-II filaments spans the apical region of mesothelium. Structured illumination microscopy of mesothelium expressing MRLC-GFP, with detailed view in (c') (d) Myosin-II filaments intensification precedes apical constriction. Representative temporal changes in myosin-II filaments intensity at the apical cortex and size of mesothelial cell apical area.

(e,f) Spheroid contracts basal substrate inwards. Time lapse images(e) and quantification(f) of radial traction stress of E-cad GFP expressing spheroid attaching onto the PDMS substrate.

(g,h,i) Traction force of mesothelial cells did not exhibit obvious changes upon fracture. Time lapse images (g) and quantification of average traction stress (h) and radial traction stress (i) of EcadtdT expressing mesothelium when invaded by spheroid expressing E-cad GFP.

All data are means ± SEM from n=7 cells from at least 3 independent experiments, except for (b) which is from 4 independent experiments, analysed with Mann Whitney U test. Scale bars, 5μm.

Figure 3. Intercellular integrin adhesion and fibronectin matrix complexes connecting spheroid to the mesothelium.

(a) Strands of integrin adhesion clusters at the spheroid-mesothelium interface from spheroid expressing paxillin GFP with indicated XZ representative views (bottom).

(b) The spheroid leader cell's Paxillin GFP clusters growth at the spheroid-mesothelium interface. The cell that is first attached to the mesothelium is defined as the invasion leader cell. Time-lapse imaging of Paxillin GFP at the spheroid-mesothelium interface.

(c) Cadherin at the interface between spheroid (top left, brightfield) expressing E-cad GFP and mesothelium expressing E-cad tdTomato does not colocalize, with detailed views of c' in c'' and c'''.

(d) Representative fluorescence line-scan analysis of spheroid E-cad GFP and mesothelium E-cad tdTomato in c''' reveals a lack of homophilic E-cadherin interactions.

(e) Thrombospondin-1 peptide treatment prevents spheroid-induced mesothelial fracture. Rate of spheroid-induced fracture in control compared to thrombospondin-1 peptide treated cultures.

(f,g) Spheroid integrin knockdown blocks fracture. Representative images (e) and quantification of the spheroid (f) invading the mesothelium in control compared to ITGA5 knockdown in the spheroid.

(h) Time-lapse images of spheroid displacing mesothelial doublets from round adhesive fibronectin patterns into non-adhesive zones.

(i) Co-localization of fibronectin with apical mesothelial integrin clusters. Immunofluorescence images of immunostained fibronectin and mesothelium expressing Paxillin-GFP with detailed views (bottom).

(j) Mesothelial apical integrin adhesion complex in the absence of spheroid engagement. Immunofluorescence images of mesothelium apical region immunostained for Paxillin, ITGA5, FN1, Kank-2 and Vinculin.

(k,l) Mesothelial FN1 and ITGA5 are required for spheroid-induced mesothelial fracture. Rate of spheroid-induced fracture in control when compared to either mesothelium FN1 knockdown or ITGA5 knockdown.

(m) Design of ITGA5-GFP fused to RhoA dominant negative T19N mutant for expression in the mesothelium.

(n,o) Spheroid-induced fracture requires activation of contractility at sites of mesothelial ITGA5 adhesion. Representative images(n) and quantification (o) of spheroid-induced mesothelial fracture rate in control mesothelium expressing ITGA5 knockdown with reconstitution of ITGA5-GFP when compared to the reconstitution of ITGA5-GFP fused to RhoA dominant negative T19N mutant in the mesothelium.

All data are means ± SEM from at least with ~50 spheroid from n=3 independent experiments, $*p < 0.05$, $**p < 0.01$; analysed with unpaired t-test. Scale bars, 5μm.

Figure 4. Fluidization and directed collective motility of contact-inhibited invading spheroids.

(a) Model for spheroid induced mesothelium tensile fracture

(b,c) Mesothelium retards spheroid spreading. (b) Representative images and (c) quantification of the size of mesothelial clearance by spheroid compared to the degree of spheroid spreading without mesothelium.

(d) Representative images of a OVCA433 spheroid labelled with H2B-mNeon segmented by 3D StarDist (left) and a 3D rendering of the segmented nuclei.

(e) Representative 2D projection of a 3D cell trajectories in spheroid invading the mesothelium over time: (left) in XY axis, projected from the top, (middle) map in XZ axis projected from the side and (right) map in RZ axis, a radial projection of spheroid assuming the rotational symmetry around the axis at in-plane center of the spheroid.

(f) Spheroid cells exhibit motility bias towards the mesothelium prior to mesothelial fracture. Representative XZ and RZ side views velocity maps of a spheroid 6 and 3 minutes prior to control mesothelium fracture compared to spheroid that will not induce fracture due to ITGA5 knockdown in mesothelium.

(g) Mesothelium ITGA5 is required for spheroid cells motility bias towards the mesothelium. The ratio of spheroid cells Z velocity mean over standard deviation of XY velocities distribution of spheroid cells on control mesothelium compared to spheroid cells on ITGA5 knockdown mesothelium.

(h) Persistency of directed spheroid cell migration (see Methods) is the highest in freely spreading spheroid then spheroid invading the mesothelium and lowest in spheroid without invasion due to ITGA5 knockdown in mesothelium. Quantification of spheroid cells velocity auto-correlation persistency in freely spreading spheroid and spheroid with or without invasion.

(i,j) Pair-wise mean square displacement (MSD) (i) (see Methods) of representative samples for three conditions, namely freely spreading spheroid and spheroid with or without invasion. (j) Local slope of MSD value obtained from the pair-wise mean square displacement graph for six selected regions from top to base of spheroids (see Methods) for three different conditions.

(k) Spheroid spreading in the absence of mesothelium may experience less crowding. The ratio of the standard deviation of in-plane displacement (v_{xy}) over that of vertical displacement (v_z), with time interval dt ~10 minutes, in freely spreading spheroid is higher than spheroid with or without invasion.

(l) Cellular crowding in invaded spheroid. Normalized mean distance of nearest neighbour (see Methods) is decreasing over time in spheroid that invades the mesothelium as compared to freely spreading spheroid and spheroid that did not invade.

(m,n,o) A lower proliferation potential in spheroid cells at the base of invaded spheroid. XZ views (m), nuclear Ki67 quantification (n, spheroid lower regions) and Yap

nuclear/cytoplasmic ratio quantification (o, spheroid lower regions) of invaded spheroid and freely spreading spheroid labelled with Ki67 or Yap and DAPI, after ~ 5 hours of attachment.

All data are means ± SEM from at least n=4 independent experiments, except for (n) which are means ± SD from n=133 spheroid cells from 2 independent experiments, *$p < 0.05$, **$p < 0.01$, ****$p < 0:0001$; analysed with Mann-Whitney U test. Scale bars, 5μm.

Supplementary Figure 1.

(a) Representative image of mesothelium expressing E-cad GFP wild-type and Ecad GFP fused with RhoA-T19N, immunostained for phospho-myosin light chain(red).
(b) Spheroid's rate of invading either mesothelium expressing wild-type E-cadherin or E-cadherin fused with RhoA-T19N.
(c) Quantification of spheroid protrusions before and after fracture.

All data are means ± SEM from n=8 independent experiments, ns, not significant; analysed with unpaired t-test. Scale bars, 5μm.

Supplementary Figure 3.

(a) Additional representative image of XZ views of a spheroid cell's Paxillin-GFP clusters on a mesothelium expressing E-cadherin tdTomato.
(b) Spreading of a spheroid leader cell on a mesothelial cell is sufficient for mesothelial fracture. Quantification of the number of spheroid cell spreading on the mesothelium prior to spheroid induced mesothelial fracture.
(c) Blocking of integrin to fibronectin interactions with TSP-1 inhibits spheroid invasion. Representative image of spheroid invading mesothelium in control compared to when TSP-1 is introduced.
(d) Immunoblot of α5 integrin knockdown in OVCA433 spheroids with α−Tubulin as loading control.
(e) Mesothelial cells remained attached on the adhesive fibronectin round pattern in the absence of invading spheroids. Time-lapse imaging of mesothelial cells expressing E-cadherin tdTomato and cytoplasmic GFP on fibronectin round patterns.
(f) Immunoblot of fibronectin knockdown in mesothelium with α−Tubulin as loading control.

(g) Knockdown of mesothelium fibronectin inhibits spheroid invasion. Representative image of spheroid invading mesothelium in control compared to when fibronectin-1 is knocked down in the mesothelium.

(h) Knockdown of α5 integrin is most prominent at the apical region of mesothelium. Representative images of mesothelium with α5 integrin knockdown at the apical and basal region, immunostained with α5 integrin and Paxillin.

(i) Knockdown of mesothelial α5 integrin inhibits spheroid invasion. Representative image of spheroid invading mesothelium in control compared to when α5 integrin is knocked down in the mesothelium.

(j,k) Immunoblot of GFP, RhoA and GAPDH loading control of mesothelial cells expressing ITGA5-GFP and ITGA5-GFP fused with RhoA-T19N.

(l) ITGA5-GFP fused with RhoA-T19N reduces apical phosphoMLC. Mesothelial cells expressing ITGA5-GFP and ITGA5-GFP fused with RhoA-T19N immunostained for phosphoMLC.

Supplementary Figure 4.

(a, b) Representative XY top view, XZ and RZ side views of spheroid cells tracks of that did not invade the mesothelium (a) and freely spreading spheroid (b) over time.

(c) Yap is localized in the cytoplasm of the spheroid that invaded the mesothelium. Representative XZ view of invaded spheroid and freely spreading spheroid immunostained with Yap and DAPI, after ~ 5 hours of attachment.

Supplementary Videos

Video 1. Formation of fibrillar bridges and microvoids at mesothelial E-cadherin (hot orange) cell-cell contacts during spheroid invasion.

Video 2. Formation of fibrillar bridges (Ecad tdTomato, red) and microvoids at mesothelium (GFP, green) grown on matrigel during spheroid invasion.

Video 3. Opposite sliding of mesothelial cell-cell contacts (Ecad tdTomato, red) during fracture propagation by spheroid invasion.

Video 4. Apical constriction of mesothelial cell expressing myosin regulatory light chain (MRLC-GFP, green) and E-cadherin tdTomato (red) during spheroid invasion.

Video 5. Representative multi-panel videos of spheroid invasion of the mesothelium, in the three following experimental conditions. 1) Fibronectin-1 and 2) α5 integrin siRNA mediated knockdown in mesothelium compared to controls. 3) Mesothelium expressing α5 integrin GFP fused with RhoA-T19N compared to control mesothelium expressing wild-type α5 integrin GFP. Arrows indicate four ends of the widening hole led by mesothelium fracture overtime.

Video 6. Representative multipanel video of mesothelial (E-cad tdT, red) clearance by spheroid (E-cad GFP, green/brightfield, grey)

Video 7. Representative multipanel video of freely spreading Ecad-GFP(green) spheroid (brightfield, grey).

Video 8. Representative multipanel video of spheroid expressing H2B-mNeon invading Ecad-tdT expressing mesothelium and the corresponding XZ and RZ velocity maps on the right.

Acknowledgements

We gratefully thank Hui Ting Ong, Chaoyu Fu, Ti Weng Chew, Xingyu Xia, Yukako Nishimura, Thuan Beng Saw and Alexander Bershadsky for their unstinting support and advice during this project. Wei Jia Goh for discussions and suggestions on 3D StarDist. We gratefully thank Tay Shu Chian for editing the manuscript. We gratefully thank Diego Pitta de Araujo for making the illustration diagrams. We gratefully thank Ince Tan for providing the ZT-GFP cells. **Funding:** This research was supported by a Young Individual Research Grant (MOH Grant No: MOH-OFYIRG20nov-0019) by the National Medical Research Council of Singapore to SKW. A Research Scholarship Block Research Fellow Scheme by the Singapore Ministry of Education to S.K.W and B.C.L. Y. L. thanks the financial support from the Research Grants Council (Project No.: GRF/17210618, GRF/17210520) of the Hong Kong SAR Government and the National Natural Science Foundation of China (Project No. 12272332). A Singapore Ministry of Education Academic Research Fund Tier 3 (MOE Grant No: MOE2016-T3-1-002) to BCL and Mechanobiology Institute's seed fund to BCL and T.H. **Competing Interests:** Authors declare no competing interests.

Author Contributions

S.K.W and B.C.L conceived the project. SKW and C.Z.H performed all experiments except for traction force microscopy and immunoblotting, which were shared with J.X and C.B.H. F.Q.S and Y.L conducted fracture analysis. T.H and Y.L conducted spheroid fluidization and crowding analysis ; C.B.H, I.Y and M.S contributed to traction force analysis and 3D StarDist A.I based nucleus segmentation. S.V and A.S.Y provided input on cadherin and myosin experiments. A.S.Y and Y.L edited the manuscript. J.C contributed to imaging setup. All analysis were performed with S.K.W assisted by C.Z.H. All authors feedback on the manuscript.

Methods

Cell culture OVCA433 ovarian cancer cell lines and the ZT mesothelial cells were cultured in a 1:1 ratio of medium MCDB 105 (Cell Applications Inc.) and Medium 199 (GIBCO) supplemented with 10% FBS (GIBCO). The OVCA433 cell lines were obtained from Michael Sheetz's laboratory. ZT mesothelial cells were obtained from a benign pleural effusion, a gift from Ince Tan. These cells were immortalized by ectopic expression of SV40 T antigen and overexpression of human telomerase (fused to GFP), as previously described [9]. Non-GFP expressing ZT cells were obtained by sorting out non-fluorescence ZT cells and they were subsequently immortalized by transfecting them with SV40 T-antigen expressing plasmid (Addgene).

Heterotypic spheroid-monolayer coculture IWAKI 35mm dishes (12mm glass diameter) were coated with 1:100 Human Fibronectin plasma (Sigma-Aldrich) in PBS and incubated at 4°C overnight. Subsequently, ZT mesothelial cells were seeded and incubated at 37°C to form a confluent monolayer.

Spheroids of OVCA433 were prepared by dissociating cells with trypsin-free Cell Dissociation Buffer, PBS (Gibco) and incubated in suspension in 2ml of 1:1 ratio of medium MCDB 105 (Cell Applications Inc.) and Medium 199 (Gibco) with 10% FBS (Gibco) for 30 mins twice at 37°C to remove trace amounts of cell dissociation buffer and promote spheroid formation. Spheroids were transferred to a dish containing a confluent monolayer and incubated for 15 min to allow spheroids to settle prior to live imaging. Imaging was performed using Nikon W1 Spinning Disk confocal microscope with the integrated Perfect Focus System on a 60x water-immersion magnification objective. Brightfield, GFP, and RFP images were captured every 3 min for 12 h. Spheroids that invaded the monolayer were quantified by viewing data obtained

using MetaMorph Microscopy Automation and Image Analysis Software after live imaging. To quantify the mesothelial clearance area, the non-fluorescent area, created by the invading spheroid, in the GFP mesothelial monolayer images was measured at 24 h and divided by the initial area of the cancer spheroid at time 0. All measurements were taken using ImageJ software.

Plasmids, siRNA and shRNA For the expression of fluorescence transgenes we subcloned shRNA-resistant transgene fused with the fluorescence tag into the multiple cloning site of either lentiviral pLL3.7 or pLL5.0 vectors by recombination. To prevent overexpression artefacts, the shRNA targeting the corresponding endogenous proteins are cloned into the lentiviral pLL vectors between the XhoI and HpaI restriction sites. The fluorescent transgenes are designed to be shRNA resistant either by using a non-human transgene or by codon change with site-directed mutagenesis. The lentiviral constructs generated are as follows: 1. pLL3.7 human Paxillin shRNA knockdown reconstituted with gallus gallus Paxillin GFP. pLL3.7 Paxillin shRNA/gallus gallus Paxillin-GFP, 2. pLL5.0 human ITGA5 shRNA knock down reconstituted with shRNA resistant human ITGA5-GFP -- pLL5.0 human ITGA5 shRNA/shRNA resistant human ITGA5-GFP. Additionally, a linker (5′ - GGGTCTACATCTGGATCTGGGAAGCCGGGTTCTGGTGAGGGTTCT-3′) is fused between fluorescence transgenes and the RhoA dominant negative mutants for the following constructs. 3. pLL5.0 human ITGA5 shRNA knock down reconstituted with siRNA resistant human ITGA5-GFP fused to a linker and RhoA-T19N pLL5.0 human ITGA5 shRNA/shRNA resistant human ITGA5-GFP-RhoA-T19N, 4. pLL5.0 human E-cadherin shRNA knock down reconstituted with mE-cadherin-GFP fused to a linker and RhoA-T19N pLL5.0 E-cadherin shRNA/mEcad–GFP-RhoA-T19N.

The following constructs were published previously. 1. pLL5.0 Myosin Regulatory Light Chain-GFP, 2. pLL5.0 human E-cadherin shRNA knockdown reconstituted with mE-cadherin-tdTomato and 3. pLL5.0 E-cadherin shRNA/mEcad–GFP used was as previously described[21], 4. Lentiviral H2B-mNeon is a gift from Rong Li's lab.

Fibronectin 1 and Integrin alpha-5 were silenced by siRNA directed against human ITGA5 5'-GGACCAGGATGGCTACAATGA-3' and Dharmacon Smartpool siRNA directed against human FN1(5'-GCAGCACAACUUCGAAUUA-3' ; 5'-GAAAUAGAUGCAACGAUCA-

3'; 5'-GAGGAAAUCUGCACAACCA-3'; 5'-CCUAAAGACUCCAUGAUCU-3') respectively.

Protein coupling of microbeads PolyLink Protein Coupling Kit (Polysciences, Inc) was used to prepare 50µl of fluorescence beads solution. 200µg of Wheat Germ Agglutinin was added to the activated beads suspension and incubated for 2 hr at room temperature. Subsequently, the beads suspension was sonicated for 15 min and immediately added to a dish containing a confluent monolayer and centrifuged until no floating beads can be observed. Prepared OVCA433 spheroids were transferred to the dish and incubated for 15 min to allow spheroids to settle prior to live imaging.

Multi-cellular spheroids of OVCA433 were prepared by dissociating cells with trypsin-free Cell Dissociation Buffer, PBS (Gibco) and incubated in suspension in 2ml of 1:1 ratio of medium MCDB 105 (Cell Applications Inc.) and Medium 199 (Gibco) with 10% FBS (Gibco) for 30 mins twice at 37°C to remove trace amounts of cell dissociation buffer and promote spheroid formation. Spheroids were transferred to a dish containing a confluent monolayer and incubated for 15 min to allow spheroids to settle prior to live imaging. Imaging was performed using Nikon W1 Spinning Disk confocal microscope with the integrated Perfect Focus System, on the 60x water-immersion magnification objective. Brightfield, GFP, and RFP images were captured every 3 min for 12 h. Spheroids that invaded the monolayer were quantified with MetaMorph.

Computational fracture analysis of microbeads Analysis of microbeads at regions of mesothelial fracture was performed as previously described with minor modifications and additional quantifications[25]. Particle image velocimetry (PIV) analysis (PIVlab package[53] in MATLAB) was used to quantify the flow fields in the top-viewed cell layer microbeads time-lapse datasets. The PIV analysis is carried out for specific duration segments of these datasets where the field of view is fixed. The time interval of each slice is 30 seconds. We then carry out the PIV analysis by dividing the images into 64×64 pixel interrogation windows with 50% overlap on the first pass, 32×32 pixel interrogation windows with 50% overlap for the second pass, and 16×16 pixel interrogation windows with 50% overlap for the third pass. Next, we select velocity threshold limits for post-processing the resulting velocity vector fields, smooth the data and use bicubic interpolation for missing vectors. After calibrating the results, velocity

magnitude ($v = \sqrt{v_x^2 + v_y^2}$), normal strain rate [$\dot{\varepsilon} = \partial_x v_x - \partial_y v_y$][28] and shear strain rate [$\dot{\gamma} = \partial_x v_y + \partial_y v_x$] were calculated, where x and y are the directions of vectors while v_x and v_y represent the corresponding mesothelium velocity components[25].

Traction force microscopy TFM substrate was prepared as previously described [54] with minor modifications. Briefly, PDMS with an average stiffness of 15 kPa was prepared by dispensing 40 µL of 1:1 CyA and CyB mixture on the 14 mm well of the 35 mm glass bottom dish (Cellvis), spin-coating the dish at 1000 rpm for 1 min and letting it cure at 80°C for 2 h. PDMS surface was then silanised with 5% APTES in absolute ethanol, functionalised with filtered and sonicated 0.2% (v/v) 0.2 µm dark red fluorescent carboxylate-modified microspheres (FluoSpheres). Beads were inactivated by 0.1M Tri's treatment for 10 min. The substrate was coated with 100 µg/mL of poly-D-lysine for 1 hour, followed by the addition of 50 µg/ml (1:100) of human plasma fibronectin (Sigma-Aldrich) for overnight incubation at 4°C.

Subsequently, ZT mesothelial cells were seeded and incubated at 37°C to form a confluent monolayer. Multi-cellular spheroids of OVCA433 were prepared and transferred to the confluent monolayer and incubated for 15 min to allow spheroids to settle prior to live imaging. Imaging was performed using Nikon W1 Spinning Disk confocal microscope with the integrated Perfect Focus System on the x60 water magnification objectives. After 12 h, 10% SDS was added to remove cells and the substrate was left alone to recover to the resting state for an hour prior to acquiring reference images.

TFM Analysis The fluorescent bead images were maximum projected for each timepoint, and subsequently contrast-enhanced and registered to the maximum projected reference images using MultiStackReg. PIVlab[55] add-on for MATLAB was used to calculate the displacement field from the registered bead images using three passes of cross correlation with the interrogation windows as followed: 128(64), 64(32), and 32(16). Outlier vectors with abnormally large values were removed post-processing. FTTC, an ImageJ plugin for a Fourier transform-based, semi-infinite half space method was used to reconstruct force field from the displacement field[56]. Customised codes were written to generate the force map or superimpose the traction force over the cell image. For downstream analysis requiring quantification for each cell, a code was customised to import ImageJ ROIs into MATLAB to calculate the

parameters for each ROI. Radial traction stress is analysed as previously described[57]. Statistical analysis was performed using one-way ANOVA in GraphPad Prism.

Immunofluorescence and microscopy Cells were fixed at 4 ◦ C with either −20 ◦C methanol on ice for 5 min or with 4% paraformaldehyde in cytoskeleton stabilization buffer (10 mM PIPES at pH 6.8, 100 mM KCl, 300 mM sucrose, 2 mM EGTA and 2 mM MgCl2) on ice for 20 min and subsequently permeabilized with 0.2% Triton-X in PBS for 5 min at 4 ◦C.

For structured illumination microscopy, spinning-disc confocal microscopy (Yokogawa) coupled with the Live SR module (GATACA Systems), Nikon Eclipse Ti-E inverted microscope with Perfect Focus System, controlled by MetaMorph software (Molecular device) supplemented with a 100x oil 1.45 NA CFI Plan Apo Lambda oil immersion objective and sCMOS camera (Prime 95B, Photometrics)

For lattice light sheet microscopy, Zeiss Lattice Lightsheet 7 equipped with a 10x 0.4 NA illumination objective at 30º angle to cover glass and a 48x 1.0 NA detection objective at 60º angle to cover glass. Pre-defined Sinc3 beams with 30µm length x 1000nm thickness were used for image acquisition. Images were captured with Pco.edge 4.2 CLHS sCMOS camera and processed with Lattice Lightsheet 7 Processing Module.

Antibodies and blocking peptide Primary antibodies in this study were: mouse monoclonal antibody against human Fibronectin (1:100; BD Transduction Laboratories; catalogue number 610077); mouse monoclonal antibody against human CD49e/Integrin α5 Chain (1:1000 for western blotting; BD Pharmingen; catalogue number 555614) ; mouse monoclonal antibody against human Integrin alpha-5 (1:100 for immunofluorescence; EMD Millipore; catalogue number MABT201, clone number SNAKA51); rabbit monoclonal antibody [Y113] against mouse and human Paxillin alpha, beta, and gamma isoforms (1:200 for immunofluorescence; Abcam; catalogue number ab32084); mouse monoclonal antibody against GAPDH (1:1000 for western blotting; Santa Cruz Biotechnology; catalogue number sc-32233); rabbit polyclonal antibody against non-muscle myosin heavy chain IIA (1:200 for immunofluorescence; Sigma-Aldrich; catalogue number M8064)

Generation of micropatterned substrates Micropatterned substrate was fabricated by stencil patterning. Polydimethylsiloxane (PDMS) (Sylgard 184 kit, Dow Corning) was applied onto a photoresist mould, containing circular micropatterns. A mixture of elastomer to crosslinker in a 10:1 ratio (w/w) was used, followed by curing at 80°C for 2 hours. The resulting crosslinked PDMS layer was carefully detached and stamps were manually crafted. Inverting the PDMS stamp, it was positioned on an uncoated 35mm μ-dish (ibidi GmbH) with hydrophobic properties. Next, Norland Optical Adhesive 73 (NOA-73, Norland Inc.) was applied along one edge of the stamp. Through capillary action, NOA-73 flowed into the gaps between the PDMS stamp and the dish, effectively sealing the stamp on all sides. Curing the NOA-73 stencil took place under ultraviolet light for 15 seconds. Following removal of the PDMS stamp, the stencil and dish were subjected to incubation with fluorescence fibrinogen mixed fibronectin at 50 μg/ml concentration in PBS. This incubation occurred overnight at 4°C following a brief degassing at 10 mbar. After the incubation, the fibronectin solution was removed, and the stencil was detached. The dish's printed bottom was treated with 0.2% Pluronic acid-H2O for 30 minutes as a passivation step. Finally, the passivated dishes underwent three washes with PBS prior to cell seeding.

Image Processing and Analysis The images presented were processed with ImageJ (http://rsb.info.nih.gov/ij/). For quantification of apical fluorescent density and line-scan analysis, the mean intensity of the selected apical region was measured from the microscopy images. Line-scan analysis was performed as described previously[58].

For quantification of crazing, timelapse image stacks of mesothelial monolayer were analysed using Metamorph with Z-projection. Mesothelial monolayers were first visually verified to be intact prior to tearing. Timeframes showing the initial cell-cell contacts breakdown were then determined after playing through each movie and visually assessed for multiple fibrillar bridges and microvoids indicative of crazing.

ImageJ macros for image processing and analysis generated previously[59] were used to quantify the nuclear to cytoplasmic ratios of YAP fluorescence intensity and Ki-67 mean nuclear intensity in cells. For the quantification of Ki-67 mean nuclear intensity, a nuclei mask was generated from the Z-projection of DAPI for nuclear intensity quantification.

For the quantification of nuclear and cytoplasmic mean fluorescence intensity of YAP, a nuclei mask from Z-projected image stacks of DAPI, and 1 μm of the surrounding region around the nucleus was selected and designated as the cytoplasmic region. To ensure the separation of overlapping nuclei, watershed function was applied on the nuclei mask. Background values were quantified in regions without cells and subtracted from the respective quantified intensities.

Spheroid nucleus segmentation with StarDist 3D deep learning model and cell tracking by IMARIS The image stacks of the spheroids underwent manual labelling through the utilization of the Labkit plugin in ImageJ. These labels were subsequently employed as the ground truth masks for the StarDist 3D segmentation. A subset of the labelled stacks, selected at random, was allocated for both training (N_train=19) and testing (N_test=2) datasets. To augment the data, various techniques, including random flips, rotations, and intensity modifications, were applied during training to effectively expand the pool of training examples. The initial model parameters were set using the pre-trained StarDist model weights[60].

Throughout the training process, the last five Conv3D layers of the model were reinitialized and trained over 100 epochs. A learning rate of 10^{-4} was employed, along with a patch size of 8x96x96. All other training parameters were kept consistent as previously[60]. Following this, the best-performing model, determined by the lowest test dataset loss, underwent further fine-tuning for an additional 10 epochs. During this fine-tuning phase, a reduced learning rate of 10^{-6} was employed. All training and fine-tuning procedures were executed on a shared Jupyter notebook server equipped with an NVIDIA RTX 6000 GPU.

After model training, the trained model was deployed for predictions on new spheroid images. This inference step was carried out using a Google Colab notebook with GPU acceleration. After executing the prediction code, the resultant labels were compared with the original image stack to assess segmentation accuracy. Following this evaluation, the autoregressive motion algorithm was applied to enable automated tracking of the segmented H2B mNeon nuclei time-lapse images in IMARIS, resulting in the generation of nuclei tracks. These tracks were then subjected to manual refinement across all frames to accurately capture the movement of spheroid cells.

Pair-wise mean square displacement (MSD) analysis of cell nucleus Given a time t, the distance of two nuclei i and j is denoted as $\Delta x_{i,j}(t)$. The displacement of this distance over an time interval dt is $\Delta x_{i,j}(t, dt) = \Delta x_{i,j}(t+dt) - \Delta x_{i,j}(t)$. Then, the pair-wise MSD $\langle \Delta x^2 \rangle (dt)$ is the squared distance averaged over all time points and all nuclei pairs. MSD increases with dt with a power $\langle \Delta x^2 \rangle \propto dt^{\sigma}$, where $\sigma(dt) = \partial \ln \langle \Delta x^2 \rangle / \partial \ln dt$, is referred to as local slope in the main text. This local slope is 1 across all timescale dt, if the particles move by random diffusion.

Cell migration persistency analysis Let $\boldsymbol{x_i}$ be the position of cell nuclei i in the XYZ (Cartesian) coordinate space, where the origin of the space $\boldsymbol{x}_0 = \langle \boldsymbol{x} \rangle$ is the averaged positions of all cells in spheroids. Then, the velocity of nucleus i is calculated as the distance of the nucleus between two consecutive frames: $\boldsymbol{v}_i(t) = \boldsymbol{x_i}(t+dt) - \boldsymbol{x_i}(t)$, where $dt = 3$ minutes, the time resolution of tracking. The direction of the velocity is $\hat{v}_i(t) = v_i(t)/|v_i(t)|$, from which the auto-correlation of velocity directions $C(dt) = \langle \hat{v}_i(t) \hat{v}_i(t+dt) \rangle$ could be obtained. The decay of C with the lag time dt follows an exponential form as $C \propto \exp(-dt/\tau)$, where τ is the persistent timescale.

Z-stacks of spheroid Let S be the total number of stacks to be sliced and each stack is enumerated as integer s ranging from 1 (top) to S (base). We first calculate the cumulative distribution M of the cell nuclei in the spheroid along Z direction, then M=0 corresponds to the top surface and M =1 at the bottom surface. Next, we determine the upper bound z_s and lower bound z'_s of a stack s in such a way that $M(z_s) = (s-1)/S$ and $M(z'_s) = \min(1, (s-1)/S + h)$, where h is a predefined effective thickness ($0 < h < 1$). Note that a fixed h imposes a similar number of cells within each stack and excludes the bias from the population number in the statistics. Finally, we select the cells with its vertical position z within the range of $[z_s, z'_s]$ for a stack s. In the main text, total number of stacks S is set as 6 and the effective thickness h is 0.3.

Nearest neighbour analysis Nearest neighbour distance of nuclei is the distance averaged over 5 nearest neighbour distances for each nucleus and then averaged over all nuclei in the selected region. Finally the distance is normalised by the nearest neighbour distance of the whole spheroid at the initial time point.

REFERENCES

1. Dahmann, C., Oates, A.C. & Brand, M. Boundary formation and maintenance in tissue development. *Nat Rev Genet* **12**, 43-55 (2011).
2. Wirtz, D., Konstantopoulos, K. & Searson, P.C. The physics of cancer: the role of physical interactions and mechanical forces in metastasis. *Nat Rev Cancer* **11**, 512-522 (2011).
3. Ladoux, B. & Mege, R.M. Mechanobiology of collective cell behaviours. *Nat Rev Mol Cell Biol* **18**, 743-757 (2017).
4. Cai, D. *et al.* Mechanical feedback through E-cadherin promotes direction sensing during collective cell migration. *Cell* **157**, 1146-1159 (2014).
5. Naora, H. & Montell, D.J. Ovarian cancer metastasis: integrating insights from disparate model organisms. *Nat Rev Cancer* **5**, 355-366 (2005).
6. Burleson, K.M. *et al.* Ovarian carcinoma ascites spheroids adhere to extracellular matrix components and mesothelial cell monolayers. *Gynecol Oncol* **93**, 170-181 (2004).
7. Iwanicki, M.P. *et al.* Ovarian cancer spheroids use myosin-generated force to clear the mesothelium. *Cancer Discov* **1**, 144-157 (2011).
8. Kenny, H.A. *et al.* Mesothelial cells promote early ovarian cancer metastasis through fibronectin secretion. *J Clin Invest* **124**, 4614-4628 (2014).
9. Davidowitz, R.A. *et al.* Mesenchymal gene program-expressing ovarian cancer spheroids exhibit enhanced mesothelial clearance. *J Clin Invest* **124**, 2611-2625 (2014).
10. Naffar-Abu Amara, S. *et al.* Transient commensal clonal interactions can drive tumor metastasis. *Nat Commun* **11**, 5799 (2020).
11. Perez-Gonzalez, C. *et al.* Active wetting of epithelial tissues. *Nat Phys* **15**, 79-88 (2019).
12. Morris, R.G. & Yap, A.S. Wetting by living tissues. *Nature Physics* **15**, 6-7 (2019).
13. Pallarès, M.E. *et al.* Stiffness-dependent active wetting enables optimal collective cell durotaxis. *Nature Physics* (2022).
14. Mutsaers, S.E. Mesothelial cells: their structure, function and role in serosal repair. *Respirology* **7**, 171-191 (2002).
15. Birbeck, M.S. & Wheatley, D.N. An Electron Microscopic Study of the Invasion of Ascites Tumor Cells into the Abdominal Wall. *Cancer Res* **25**, 490-497 (1965).
16. Witz, C.A., Monotoya-Rodriguez, I.A. & Schenken, R.S. Whole explants of peritoneum and endometrium: a novel model of the early endometriosis lesion. *Fertil Steril* **71**, 56-60 (1999).
17. Zhang, X.Y. *et al.* Characteristics and growth patterns of human peritoneal mesothelial cells: comparison between advanced epithelial ovarian cancer and non-ovarian cancer sources. *J Soc Gynecol Investig* **6**, 333-340 (1999).
18. Kenny, H.A., Nieman, K.M., Mitra, A.K. & Lengyel, E. The first line of intra-abdominal metastatic attack: breaching the mesothelial cell layer. *Cancer Discov* **1**, 100-102 (2011).
19. Kenny, P.A. *et al.* The morphologies of breast cancer cell lines in three-dimensional assays correlate with their profiles of gene expression. *Mol Oncol* **1**, 84-96 (2007).
20. Rottler, J., Barsky, S. & Robbins, M.O. Cracks and crazes: on calculating the macroscopic fracture energy of glassy polymers from molecular simulations. *Phys Rev Lett* **89**, 148304 (2002).
21. Smutny, M. *et al.* Multicomponent analysis of junctional movements regulated by myosin II isoforms at the epithelial zonula adherens. *PLoS One* **6**, e22458 (2011).

22. Shewan, A.M. *et al.* Myosin 2 is a key Rho kinase target necessary for the local concentration of E-cadherin at cell-cell contacts. *Mol Biol Cell* **16**, 4531-4542 (2005).
23. Wu, S.K. & Priya, R. Spatio-Temporal Regulation of RhoGTPases Signaling by Myosin II. *Front Cell Dev Biol* **7**, 90 (2019).
24. Acharya, B.R. *et al.* Mammalian Diaphanous 1 Mediates a Pathway for E-cadherin to Stabilize Epithelial Barriers through Junctional Contractility. *Cell Rep* **18**, 2854-2867 (2017).
25. Prakash, V.N., Bull, M.S. & Prakash, M. Motility-induced fracture reveals a ductile-to-brittle crossover in a simple animal's epithelia. *Nature Physics* **17**, 504-511 (2021).
26. Anderson, T.L. *Fracture mechanics : fundamentals and applications*, Edn. Fourth edition. (CRC Press/Taylor & Francis, Boca Raton; 2017).
27. Greenhalgh, E.S. *Failure analysis and fractography of polymer composites*. (Woodhead Publishing Limited : CRC Press, Cambridge, England ; New Delhi, India ; Boca Raton, Florida; 2009).
28. Stamhuis, E.J. Basics and principles of particle image velocimetry (PIV) for mapping biogenic and biologically relevant flows. *Aquatic Ecology* **40**, 463-479 (2006).
29. Sawyer, J.M. *et al.* Apical constriction: a cell shape change that can drive morphogenesis. *Dev Biol* **341**, 5-19 (2010).
30. Martin, A.C. & Goldstein, B. Apical constriction: themes and variations on a cellular mechanism driving morphogenesis. *Development* **141**, 1987-1998 (2014).
31. Martin, A.C., Kaschube, M. & Wieschaus, E.F. Pulsed contractions of an actin-myosin network drive apical constriction. *Nature* **457**, 495-499 (2009).
32. Martin, A.C., Gelbart, M., Fernandez-Gonzalez, R., Kaschube, M. & Wieschaus, E.F. Integration of contractile forces during tissue invagination. *J Cell Biol* **188**, 735-749 (2010).
33. Wu, S.K. & Yap, A.S. Patterns in space: coordinating adhesion and actomyosin contractility at E-cadherin junctions. *Cell Commun Adhes* **20**, 201-212 (2013).
34. Mason, F.M., Xie, S., Vasquez, C.G., Tworoger, M. & Martin, A.C. RhoA GTPase inhibition organizes contraction during epithelial morphogenesis. *J Cell Biol* **214**, 603-617 (2016).
35. Wu, S.K., Budnar, S., Yap, A.S. & Gomez, G.A. Pulsatile contractility of actomyosin networks organizes the cellular cortex at lateral cadherin junctions. *Eur J Cell Biol* **93**, 396-404 (2014).
36. Sonam, S. *et al.* Mechanical stress driven by rigidity sensing governs epithelial stability. *Nature Physics* **19**, 132-141 (2023).
37. Parsons, J.T., Horwitz, A.R. & Schwartz, M.A. Cell adhesion: integrating cytoskeletal dynamics and cellular tension. *Nat Rev Mol Cell Biol* **11**, 633-643 (2010).
38. Wu, S.K. *et al.* Cortical F-actin stabilization generates apical-lateral patterns of junctional contractility that integrate cells into epithelia. *Nat Cell Biol* **16**, 167-178 (2014).
39. Wu, S.K., Lagendijk, A.K., Hogan, B.M., Gomez, G.A. & Yap, A.S. Active contractility at E-cadherin junctions and its implications for cell extrusion in cancer. *Cell Cycle* **14**, 315-322 (2015).
40. Sipes, J.M. *et al.* Inhibition of fibronectin binding and fibronectin-mediated cell adhesion to collagen by a peptide from the second type I repeat of thrombospondin. *J Cell Biol* **121**, 469-477 (1993).

41. Munster, S. *et al.* Attachment of the blastoderm to the vitelline envelope affects gastrulation of insects. *Nature* **568**, 395-399 (2019).
42. Liotta, L.A. & Kohn, E. Anoikis: cancer and the homeless cell. *Nature* **430**, 973-974 (2004).
43. Weigert, M., Schmidt, U., Haase, R., Sugawara, K. & Myers, G. in Proceedings of the IEEE/CVF winter conference on applications of computer vision 3666-3673 (2020).
44. Palamidessi, A. *et al.* Unjamming overcomes kinetic and proliferation arrest in terminally differentiated cells and promotes collective motility of carcinoma. *Nat Mater* **18**, 1252-1263 (2019).
45. Ilina, O. *et al.* Cell-cell adhesion and 3D matrix confinement determine jamming transitions in breast cancer invasion. *Nat Cell Biol* **22**, 1103-1115 (2020).
46. Mongera, A. *et al.* A fluid-to-solid jamming transition underlies vertebrate body axis elongation. *Nature* **561**, 401-405 (2018).
47. Pinheiro, D., Kardos, R., Hannezo, É. & Heisenberg, C.-P. Morphogen gradient orchestrates pattern-preserving tissue morphogenesis via motility-driven unjamming. *Nature Physics* **18**, 1482-1493 (2022).
48. Szabo, B. *et al.* Phase transition in the collective migration of tissue cells: experiment and model. *Phys Rev E Stat Nonlin Soft Matter Phys* **74**, 061908 (2006).
49. Angelini, T.E. *et al.* Glass-like dynamics of collective cell migration. *Proc Natl Acad Sci U S A* **108**, 4714-4719 (2011).
50. Giancotti, F.G. Mechanisms governing metastatic dormancy and reactivation. *Cell* **155**, 750-764 (2013).
51. Enderling, H. *et al.* Paradoxical dependencies of tumor dormancy and progression on basic cell kinetics. *Cancer Res* **69**, 8814-8821 (2009).
52. Thomson, J.A. On Growth and Form. *Nature* **100**, 21-22 (1917).
53. Thielicke, W. & Stamhuis, E.J. PIVlab – Towards User-friendly, Affordable and Accurate Digital Particle Image Velocimetry in MATLAB. *Journal of Open Research Software* **2** (2014).
54. Teo, J.L., Lim, C.T., Yap, A.S. & Saw, T.B. A Biologist's Guide to Traction Force Microscopy Using Polydimethylsiloxane Substrate for Two-Dimensional Cell Cultures. *STAR Protoc* **1**, 100098 (2020).
55. Thielicke, W. & Sonntag, R. Particle Image Velocimetry for MATLAB: Accuracy and enhanced algorithms in PIVlab. *Journal of Open Research Software* (2021).
56. Tseng, Q. (Université de Grenoble, 2011).
57. Kawaue, T. *et al.* Inhomogeneous mechanotransduction defines the spatial pattern of apoptosis-induced compensatory proliferation. *Dev Cell* **58**, 267-277 e265 (2023).
58. Mangold, S. *et al.* Hepatocyte growth factor acutely perturbs actin filament anchorage at the epithelial zonula adherens. *Curr Biol* **21**, 503-507 (2011).
59. Wu, S.K., Ariffin, J., Tay, S.C. & Picone, R. The variant senescence-associated secretory phenotype induced by centrosome amplification constitutes a pathway that activates hypoxia-inducible factor-1alpha. *Aging Cell* **22**, e13766 (2023).
60. Beghin, A. *et al.* Automated high-speed 3D imaging of organoid cultures with multi-scale phenotypic quantification. *Nat Methods* **19**, 881-892 (2022).

Figure 1

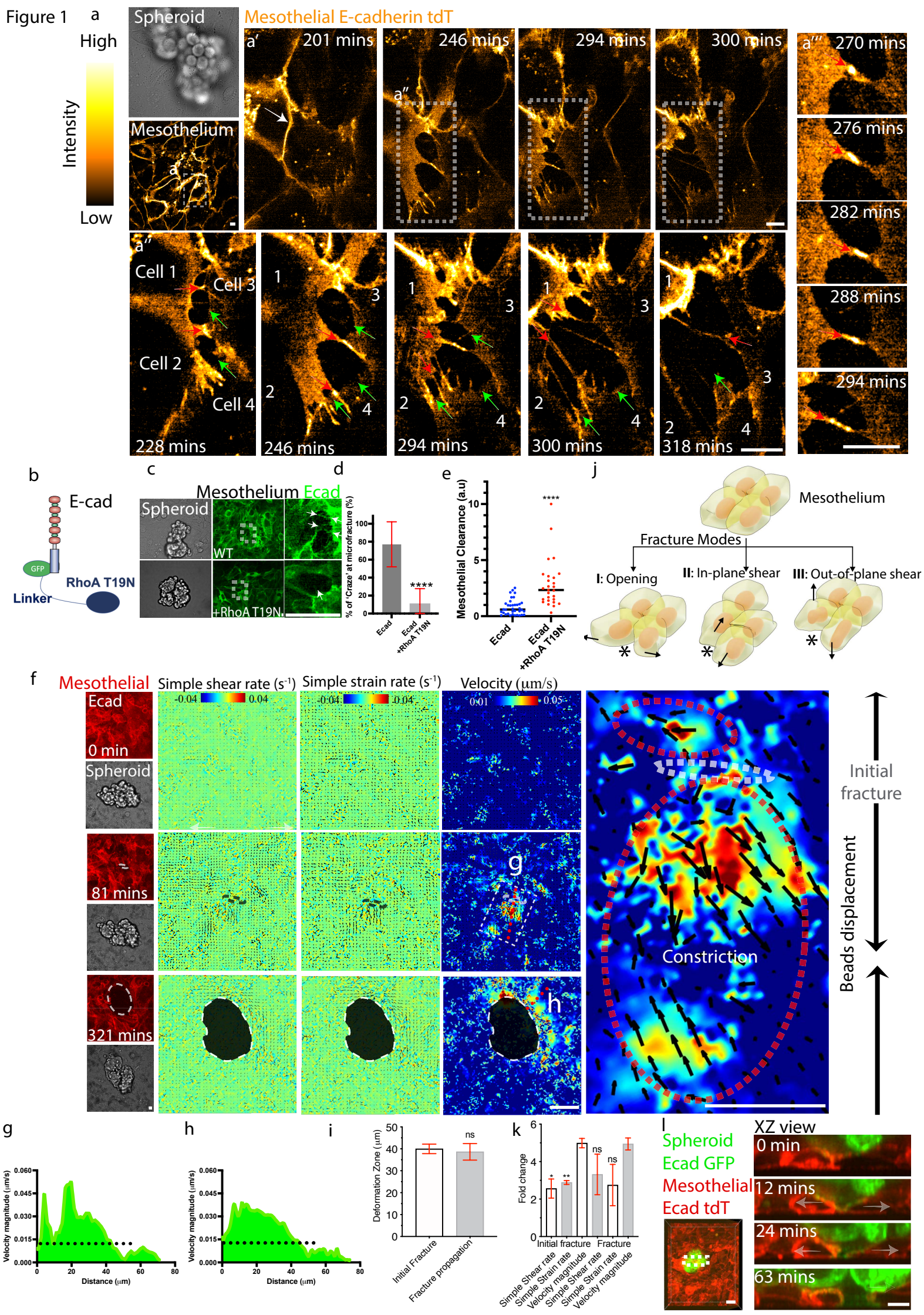
a
High
Intensity
Low
Spheroid
Mesothelium
Mesothelial E-cadherin tdT
a′
201 mins
246 mins
294 mins
300 mins
a″
a‴
270 mins
276 mins
282 mins
288 mins
294 mins
Cell 1
Cell 2
Cell 3
Cell 4
228 mins
246 mins
294 mins
300 mins
318 mins
b
E-cad
GFP
RhoA T19N
Linker
c
Mesothelium Ecad
Spheroid
WT
+RhoA T19N
d
% of 'Craze' at microfracture (%)
Ecad
Ecad +RhoA T19N
****
e
Mesothelial Clearance (a.u)
Ecad
Ecad +RhoA T19N
****
j
Mesothelium
Fracture Modes
I: Opening
II: In-plane shear
III: Out-of-plane shear
f
Mesothelial
Ecad
0 min
Spheroid
81 mins
321 mins
Simple shear rate (s⁻¹)
Simple strain rate (s⁻¹)
Velocity (μm/s)
-0.04
0.04
0.01
0.05
g
h
Constriction
Initial fracture
Beads displacement
g
Velocity magnitude (μm/s)
Distance (μm)
h
Velocity magnitude (μm/s)
Distance (μm)
i
Deformation Zone (μm)
ns
Initial Fracture
Fracture propagation
k
Fold change
Initial fracture
Fracture
Simple Shear rate
Simple Strain rate
Velocity magnitude
l
Spheroid
Ecad GFP
Mesothelial
Ecad tdT
XZ view
0 min
12 mins
24 mins
63 mins

Figure 2

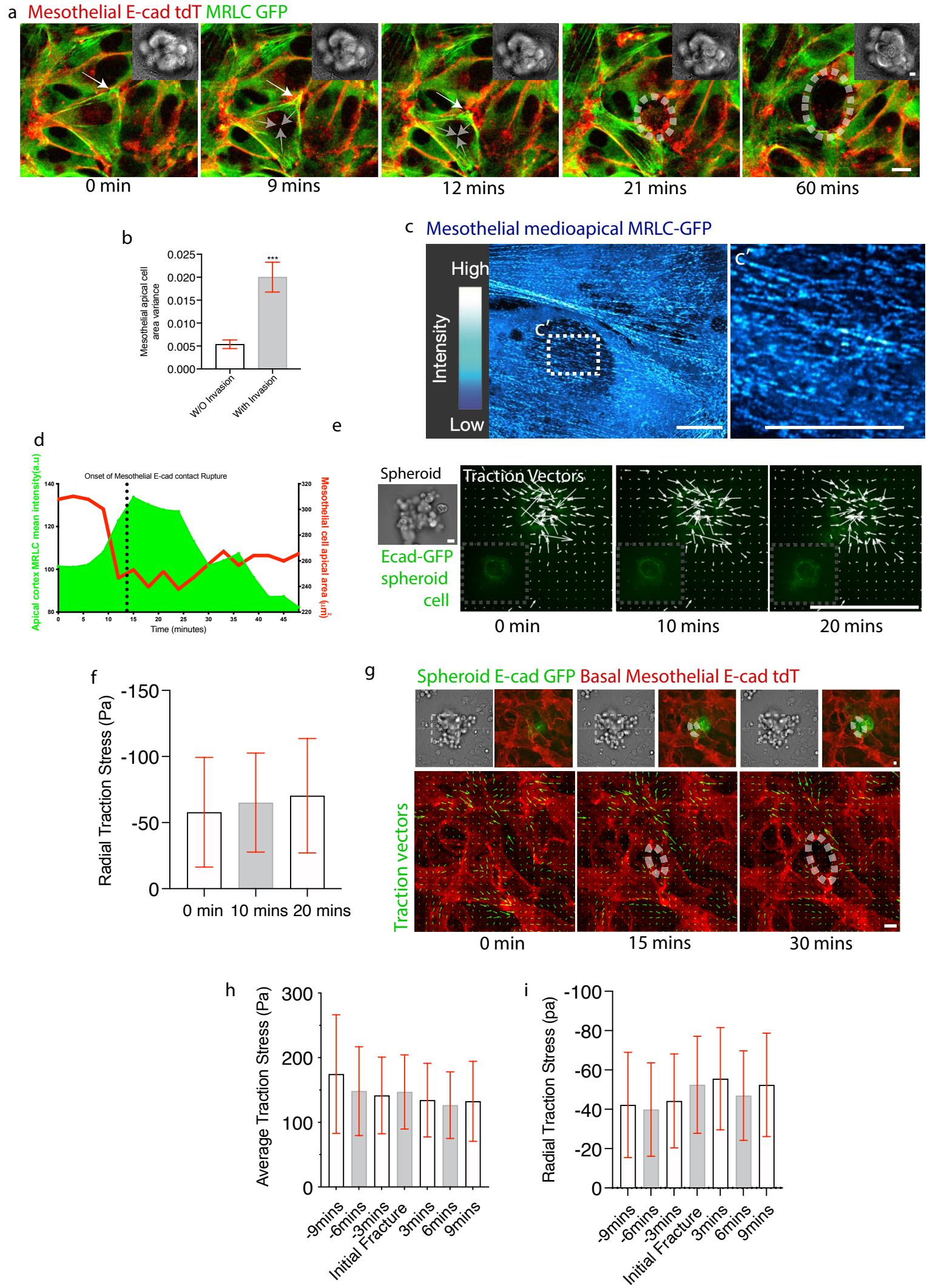
a
Mesothelial E-cad tdT MRLC GFP
0 min
9 mins
12 mins
21 mins
60 mins
b
Mesothelial apical cell area variance
0.025
0.020
0.015
0.010
0.005
0.000
***
W/O Invasion
With Invasion
c
Mesothelial medioapical MRLC-GFP
High
Intensity
Low
c′
c′
d
Onset of Mesothelial E-cad contact Rupture
Apical cortex MRLC mean intensity(a.u)
Mesothelial cell apical area (μm²)
Time (minutes)
e
Spheroid
Traction Vectors
Ecad-GFP spheroid cell
0 min
10 mins
20 mins
f
Radial Traction Stress (Pa)
-150
-100
-50
0
0 min
10 mins
20 mins
g
Spheroid E-cad GFP Basal Mesothelial E-cad tdT
Traction vectors
0 min
15 mins
30 mins
h
Average Traction Stress (Pa)
300
200
100
0
-9mins
-6mins
-3mins
Initial Fracture
3mins
6mins
9mins
i
Radial Traction Stress (pa)
-100
-80
-60
-40
-20
0
-9mins
-6mins
-3mins
Initial Fracture
3mins
6mins
9mins

Figure 3

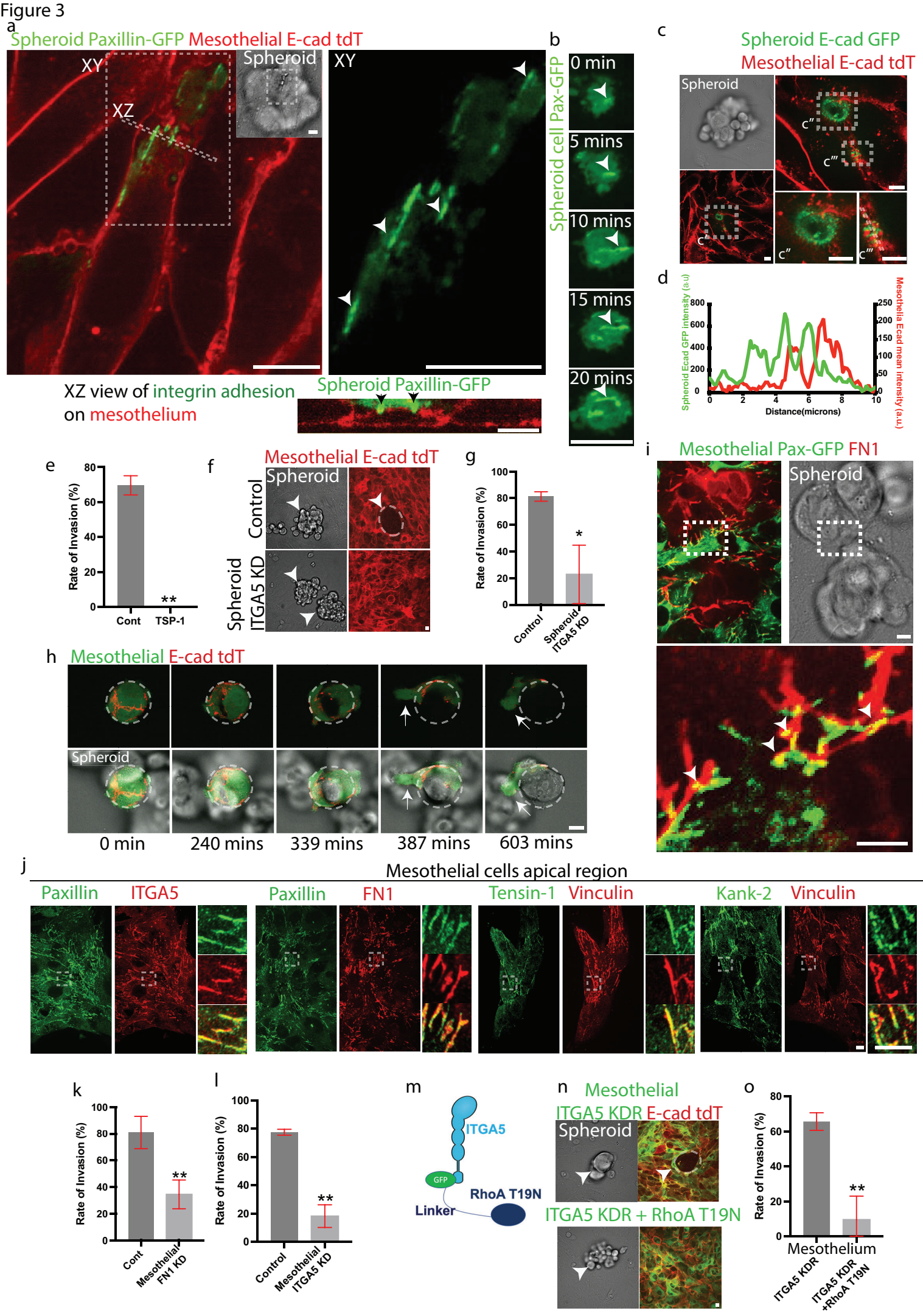
a
Spheroid Paxillin-GFP Mesothelial E-cad tdT
XY
XZ
Spheroid
XY
XZ view of integrin adhesion on mesothelium
Spheroid Paxillin-GFP
b
Spheroid cell Pax-GFP
0 min
5 mins
10 mins
15 mins
20 mins
c
Spheroid E-cad GFP
Mesothelial E-cad tdT
Spheroid
c″
c‴
d
Spheroid Ecad GFP intensity (a.u)
Mesothelia Ecad mean intensity (a.u.)
Distance(microns)
e
Rate of Invasion (%)
Cont
TSP-1
f
Mesothelial E-cad tdT
Spheroid
Control
Spheroid ITGA5 KD
g
Rate of Invasion (%)
Control
Spheroid ITGA5 KD
h
Mesothelial E-cad tdT
Spheroid
0 min
240 mins
339 mins
387 mins
603 mins
i
Mesothelial Pax-GFP FN1
Spheroid
j
Mesothelial cells apical region
Paxillin
ITGA5
Paxillin
FN1
Tensin-1
Vinculin
Kank-2
Vinculin
k
Rate of Invasion (%)
Cont
Mesothelial FN1 KD
l
Rate of Invasion (%)
Control
Mesothelial ITGA5 KD
m
ITGA5
GFP
Linker
RhoA T19N
n
Mesothelial
ITGA5 KDR E-cad tdT
Spheroid
ITGA5 KDR + RhoA T19N
o
Rate of Invasion (%)
Mesothelium
ITGA5 KDR
ITGA5 KDR +RhoA T19N

Figure 4

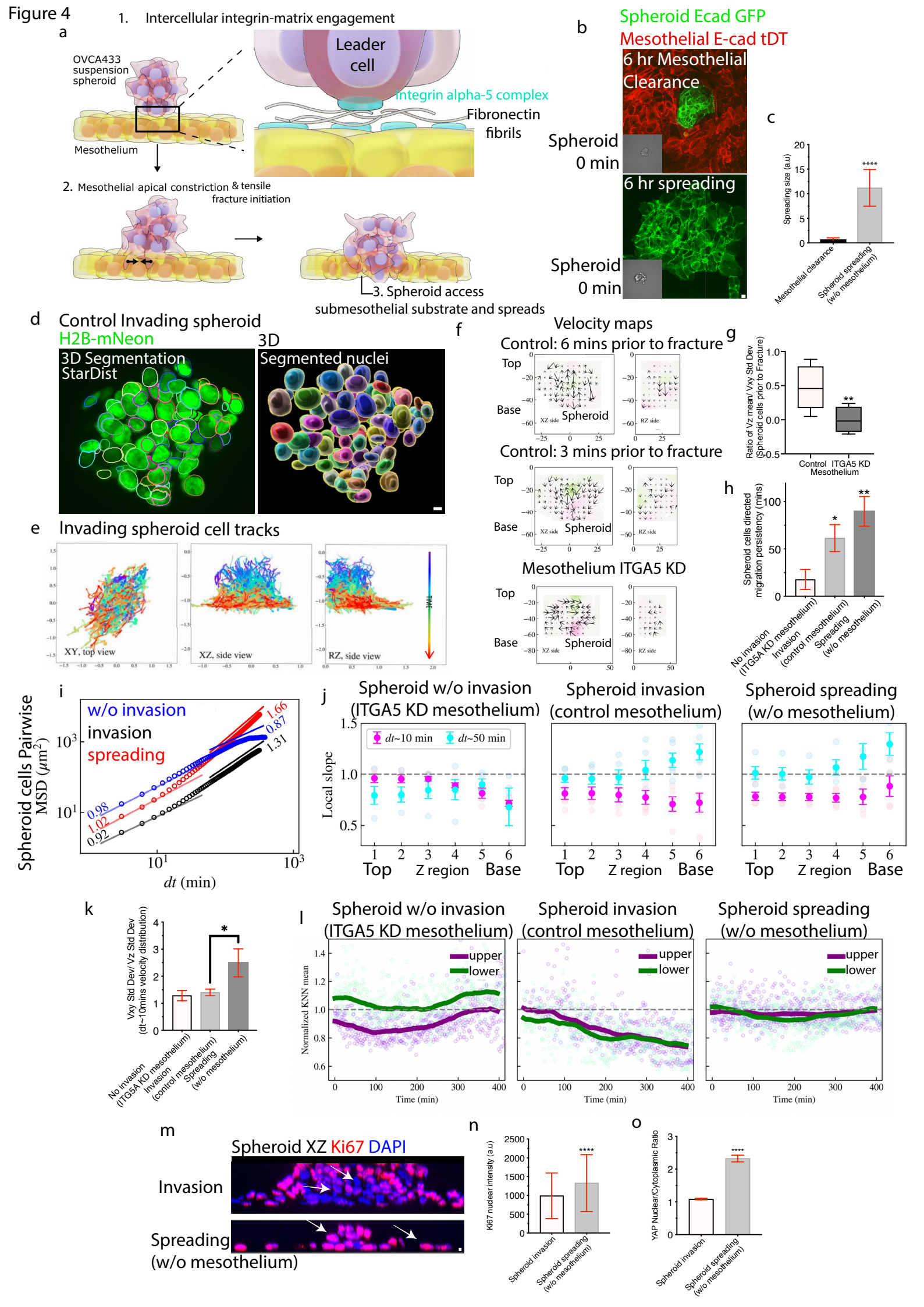
a
1. Intercellular integrin-matrix engagement
OVCA433 suspension spheroid
Mesothelium
Leader cell
Integrin alpha-5 complex
Fibronectin fibrils
2. Mesothelial apical constriction & tensile fracture initiation
3. Spheroid access submesothelial substrate and spreads
b
Spheroid Ecad GFP
Mesothelial E-cad tDT
6 hr Mesothelial Clearance
Spheroid 0 min
6 hr spreading
Spheroid 0 min
c
Spreading size (a.u)
Mesothelial clearance
Spheroid spreading (w/o mesothelium)
d
Control Invading spheroid
H2B-mNeon
3D Segmentation StarDist
3D Segmented nuclei
e
Invading spheroid cell tracks
XY, top view
XZ, side view
RZ, side view
TIME
f
Velocity maps
Control: 6 mins prior to fracture
Control: 3 mins prior to fracture
Mesothelium ITGA5 KD
Top
Base
Spheroid
XZ side
RZ side
g
Ratio of Vz mean/ Vxy Std Dev (Spheroid cells prior to Fracture)
Control
ITGA5 KD Mesothelium
h
Spheroid cells directed migration persistency (mins)
No invasion (ITG5A KD mesothelium)
Invasion (control mesothelium)
Spreading (w/o mesothelium)
i
Spheroid cells Pairwise MSD (μm²)
w/o invasion
invasion
spreading
1.66
0.87
1.31
0.98
1.02
0.92
dt (min)
j
Spheroid w/o invasion (ITGA5 KD mesothelium)
Spheroid invasion (control mesothelium)
Spheroid spreading (w/o mesothelium)
Local slope
dt~10 min
dt~50 min
Top
Z region
Base
k
Vxy Std Dev/ Vz Std Dev (dt~10mins velocity distribution)
No invasion (ITG5A KD mesothelium)
Invasion (control mesothelium)
Spreading (w/o mesothelium)
l
Spheroid w/o invasion (ITGA5 KD mesothelium)
Spheroid invasion (control mesothelium)
Spheroid spreading (w/o mesothelium)
Normalized KNN mean
upper
lower
Time (min)
m
Spheroid XZ Ki67 DAPI
Invasion
Spreading (w/o mesothelium)
n
Ki67 nuclear intensity (a.u)
Spheroid invasion
Spheroid spreading (w/o mesothelium)
o
YAP Nuclear/Cytoplasmic Ratio
Spheroid invasion
Spheroid spreading (w/o mesothelium)

Supplementary Figure 1

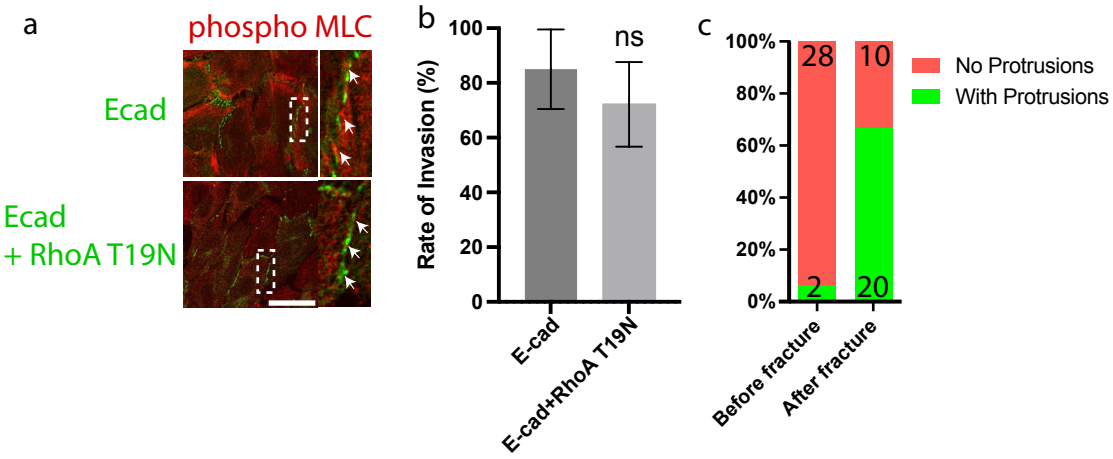

Supplementary Figure 3

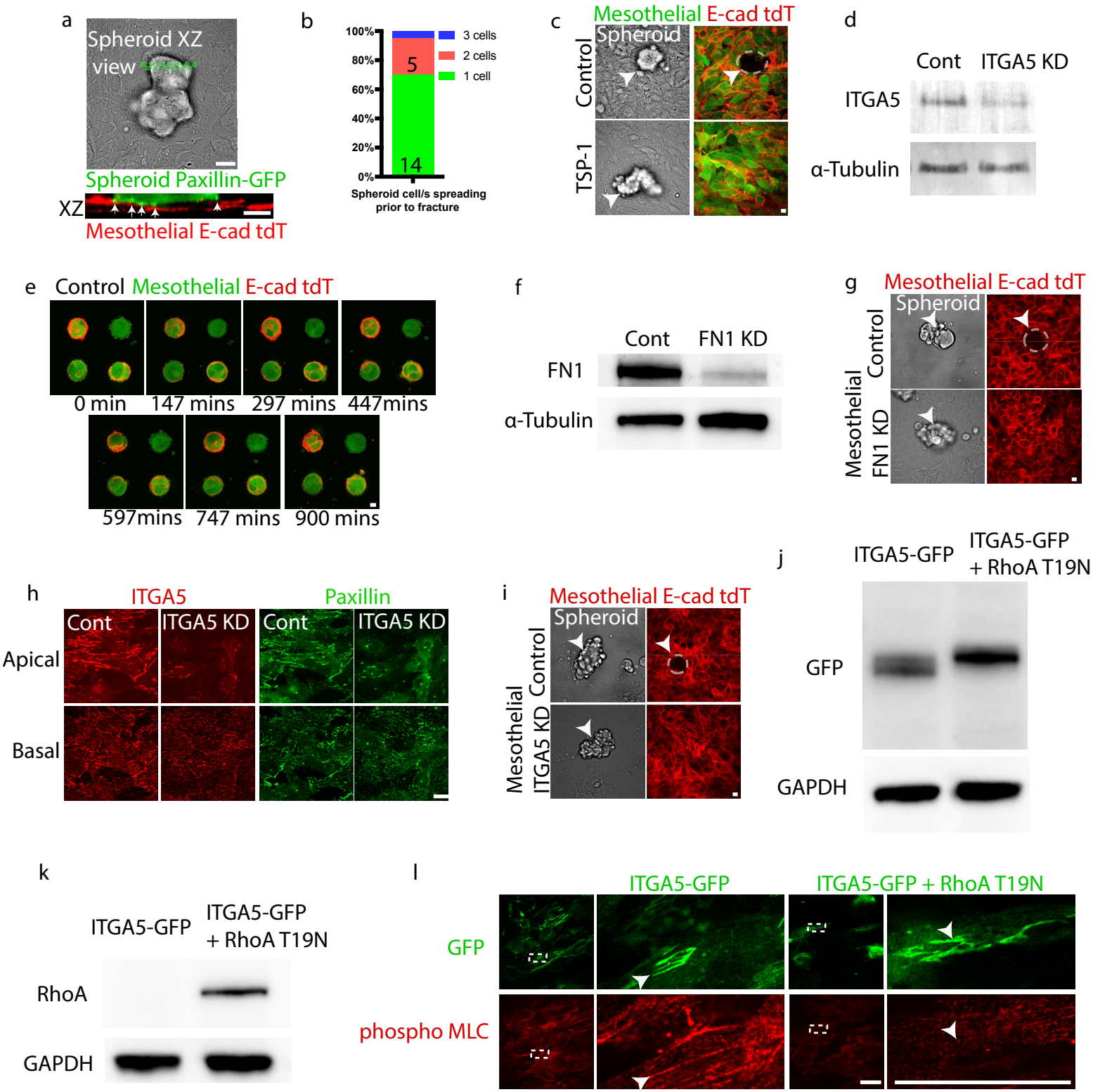

Supplementary Figure 4

a Spheroid w/o invasion cell tracks (ITGA5 KD mesothelium)

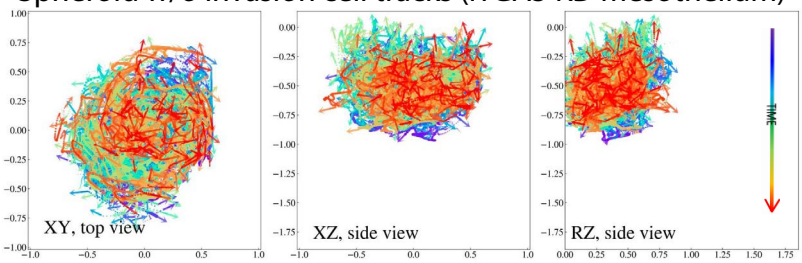

b Spheroid spreading cell tracks (w/o mesothelium)

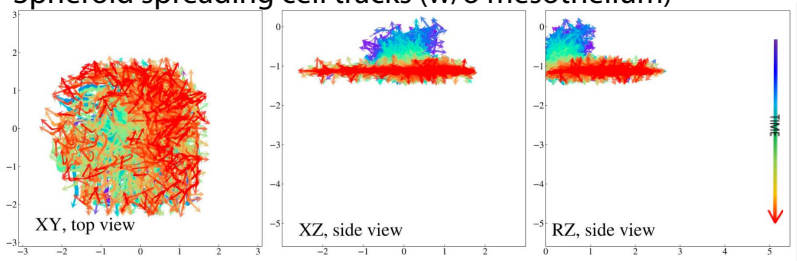

c

Spheroid XZ view Yap DAPI

Invasion

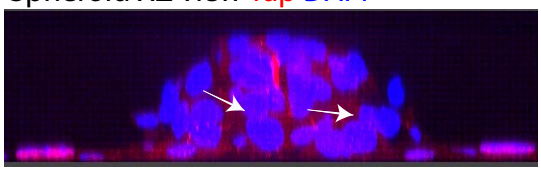
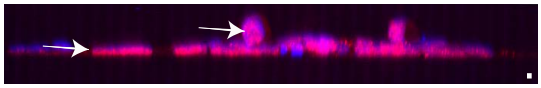
Spreading (w/o mesothelium)